Double-sided van der Waals epitaxy of topological insulators across an atomically thin membrane

Joon Young Park[1,2], Young Jae Shin[1], Jeacheol Shin[2], Jehyun Kim[2], Janghyun Jo[3], Hyobin Yoo[1,4], Danial Haei[1,5], Chohee Hyun[6], Jiyoung Yun[2], Robert M. Huber[7,8], Arijit Gupta[7,8], Kenji Watanabe[9], Takashi Taniguchi[10], Wan Kyu Park[8], Hyeon Suk Shin[11,12], Miyoung Kim[3], Dohun Kim[2], Gyu-Chul Yi[2,*], and Philip Kim[1,*]

[1] *Department of Physics, Harvard University, Cambridge, MA 02138, USA*

[2] *Department of Physics and Astronomy, and Institute of Applied Physics, Seoul National University, Seoul 08826, Republic of Korea*

[3] *Department of Materials Science and Engineering, and Research Institute of Advanced Materials, Seoul National University, Seoul 08826, Republic of Korea*

[4] *Department of Physics, Sogang University, Seoul 04107, Republic of Korea*

[5] *Center for Nanoscale Systems, Harvard University, Cambridge, MA 02138, USA*

[6] *Department of Chemistry, and Low Dimensional Carbon Materials Center, Ulsan National Institute of Science and Technology (UNIST), Ulsan 44919, Republic of Korea*

[7] *Department of Physics, Florida State University, Florida, 32306, USA*

[8] *National High Magnetic Field Laboratory, Florida State University, FL 32310, USA*

[9] *Research Center for Electronic and Optical Materials, National Institute for Materials Science, 1-1 Namiki, Tsukuba 305-0044, Japan*

[10] *Research Center for Materials Nanoarchitectonics, National Institute for Materials Science, 1-1 Namiki, Tsukuba 305-0044, Japan*

[11] *Department of Energy Science and Department of Chemistry, Sungkyunkwan University (SKKU), Suwon 16419, Republic of Korea*

[12] *Center for 2D Quantum Heterostructures, Institute of Basic Science (IBS), Sungkyunkwan University (SKKU), Suwon 16419, Republic of Korea*

[*] e-mail: gcyi@snu.ac.kr; pkim@physics.harvard.edu

Atomically thin van der Waals (vdW) films provide a novel material platform for epitaxial growth of quantum heterostructures. However, unlike the remote epitaxial growth of three-dimensional bulk crystals, the growth of two-dimensional (2D) material heterostructures across atomic layers has been limited due to the weak vdW interaction. Here, we report the double-sided epitaxy of vdW layered materials through atomic membranes. We grow vdW topological insulators (TIs) Sb_2Te_3 and Bi_2Se_3 by molecular beam epitaxy on both surfaces of atomically thin graphene or hBN, which serve as suspended 2D vdW "*substrate*" layers. Both homo- and hetero- double-sided vdW TI tunnel junctions are fabricated, with the atomically thin hBN acting as a crystal-momentum-conserving tunnelling barrier with abrupt and epitaxial interface. By performing field-angle dependent magneto-tunnelling spectroscopy on these devices, we reveal the energy-momentum-spin resonant tunnelling of massless Dirac electrons between helical Landau levels developed in the topological surface states at the interface.

Two-dimensional (2D) van der Waals (vdW) heterostructures composed of materials with various electronic properties serve as novel platforms to explore a variety of interesting physical properties and device applications[1,2]. One of the most intriguing systems is a vertical heterostructure consisting of two materials separated by an atomically thin insulating barrier, allowing vertical tunnelling transport through vdW interfaces[3-5]. Such a heterostructure with high crystal quality and epitaxial alignment is of particular interest because crystal momentum parallel to the interface can be conserved, offering a unique platform for investigating the intrinsic selection rules of the resonant tunnelling process[6-8]. The surface states of three-dimensional (3D) vdW topological insulators (TIs) of $(Bi, Sb)_2(Te, Se)_3$ compounds[9], when integrated into vdW tunnel junctions, can provide exciting opportunities to discover novel quantum phenomena occurring at the atomically sharp epitaxial interface between topologically dissimilar atomic layers[10-15].

Multilayered TI/normal insulator vdW heterostructures have been constructed by sequential direct growth using molecular beam epitaxy (MBE)[10,16]. In this conventional MBE growth, the choice of the barrier materials is constrained by chemical compatibility and lattice constant matching. Furthermore, the common occurrence of step edges during the growth process significantly reduces the effectiveness of forming a smooth vdW heterointerface.

VdW epitaxy on both surfaces of an atomically thin, single-crystalline suspended vdW membrane opens a new way to construct TI epitaxial heterostructures with atomically sharp interfaces. This novel synthesis route presented in this work distinguished from the recently demonstrated remote epitaxy of 3D/2D/3D hybrid systems. In remote epitaxial growth, the electrostatic field of the substrate (lower 3D layer) penetrates the 2D vdW interlayer (Fig. 1a)[17,18]. Due to its strong dependence on the ionic character or polarity of the 3D substrate, remote epitaxy establishes the long-range epitaxial relationship between 3D/3D bulks, insensitive to the crystallographic alignment at the 3D/2D local interfaces. On the contrary, in the newly proposed double-sided vdW epitaxy, as shown in Fig. 1b, one can utilize the short-range local vdW interaction at the interfaces, structurally connecting the top and bottom epilayers to the substrate (middle) layer. Moreover, unlike remote epitaxy where a stronger coupling leads to a stronger correlation of the electronic structure across the heterostructure, the electrical coupling can be tuned independently by the thickness and electronic properties of the middle layer. To date, while 3D/2D/3D quasi-vdW epitaxial double heterostructures have been demonstrated in the form of graphene sandwiched by semiconductor nanostructures with reconstructed dangling bonds of polar facets at the interface[19,20], all-2D double-sided vdW

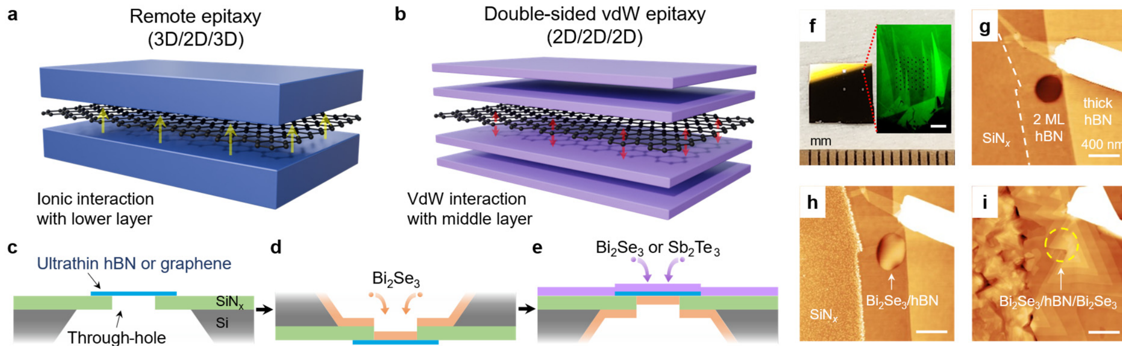

Fig. 1. Double-sided vdW epitaxy of TI/hBN(graphene)/TI vertical heterostructures. **a**,**b**, Schematics illustrating the growth mechanism of remote epitaxy (**a**) and double-sided vdW epitaxy (**b**). In remote epitaxy, the middle 2D vdW layer serves as an atomically thin spacer to mediate the long-range interaction between 3D crystals. In the new concept of double-sided vdW epitaxy, the middle vdW layer serves as an atomically thin growth template where the top and bottom layers are epitaxially connected by the short-range vdW interaction. **c**–**e**, Schematics of the double-sided vdW epitaxy procedure, where TIs are grown on the bottom and top surfaces of atomically thin vdW substrates suspended on perforated SiN_x membranes. **f**, Photograph of an array of SiN_x membrane windows compatible with MBE, TEM, and microfabrication. Inset: High-contrast optical microscope image of an array of holes fabricated in the SiN_x membrane covered by an atomically thin hBN crystal. Scale bar: 10 μm. **g**–**h**, AFM topographic images (20 nm colour scale) of 2 ML hBN suspended over one of the holes in the SiN_x membrane taken before (**g**) and after (**h**) the first growth of Bi_2Se_3 on the back side, and after the second growth of Bi_2Se_3 on the front side (**i**).

epitaxy has not yet been realized. In this Article, we present the double-sided vdW-MBE growth of 2D/2D/2D structures where two epitaxially aligned TIs are separated by atomically thin crystalline barriers with abrupt interfaces, which has enabled us to observe the resonant tunnelling between Landau levels (LLs) developed in the topological surface states (TSSs) at the vdW heterointerface where the energy, momentum, and spin of the helical Dirac fermions are conserved during the tunnelling process.

The method developed to fabricate the double-sided epitaxial vdW heterostructures is schematically illustrated in Fig. 1c–e. Ultrathin hBN layers (2–5 monolayers; MLs) or monolayer graphene are suspended over hole arrays pre-patterned in SiN_x membranes to expose both surfaces (Fig. 1f and Extended Data Fig.1). Subsequently, Bi_2Se_3 (n-type) and Sb_2Te_3 (p-type) thin films are heteroepitaxially grown on each side of the suspended layer using ultra-high vacuum (UHV) MBE (see Methods). The suspended vdW layer serves as a crystalline substrate for the epitaxy of the TI films. In particular, the atomically thin hBN layers can serve as a wide bandgap insulating barrier for tunnelling spectroscopy between the two TIs whose interface is sealed under UHV. Since the suspended vdW heterostructures are electron-transmitting and mechanically robust, this templated growth approach enables us to directly use plan-view TEM and atomic force microscopy (AFM) to study their structural properties

(Fig. 1g–i and Fig. 2) and the microfabrication processes to form electrical contacts to the junctions[21-24].

The microstructural properties of the TI/hBN(graphene)/TI heterostructures can be investigated by TEM. We first demonstrate that bottom (b-) and top (t-) Bi_2Se_3 films are epitaxially aligned through a suspended monolayer graphene, a single-atom-thick vdW crystal substrate. Figure 2a shows the plan-view selected area electron diffraction (SAED) image of the resulting heterostructure exhibiting the preferential epitaxial relationship of $\{10\bar{1}0\}_{\text{b-Bi}_2\text{Se}_3} \parallel \{10\bar{1}0\}_{\text{graphene}} \parallel \{10\bar{1}0\}_{\text{t-Bi}_2\text{Se}_3}$. The weak Bragg peaks from Bi_2Se_3 with small deviation angles can be attributed to the wrinkles formed in the suspended vdW layers (inset of Fig. 2a and ref.[23]) and to grains with a small in-plane misorientation angle, which is likely due to the weak vdW interactions at the interface[22,25-27].

The same methodology can be applied to insulating hBN substrates, which is of particular interest for vertical tunnel junctions. The cross-sectional HR-TEM image in Fig. 2b shows the quintuple layer (QL) structures of the Bi_2Se_3 thin films, and the atomically clean and abrupt interfaces between b-Bi_2Se_3, 2 ML hBN, and t-Bi_2Se_3 (see also Extended Data Fig. 2). Their epitaxial relationship can be confirmed by comparing the fast Fourier transform (FFT) of the representative areas (yellow and orange boxes) with the interfacial region (red box), where one can find matching structures of b- and t-Bi_2Se_3 (white arrows) relative to the hBN atomic registry (red arrows).

Next, we present the growth of dissimilar TI materials—namely Bi_2Se_3 and Sb_2Te_3—across a suspended hBN, further demonstrating the power of our double-sided vdW epitaxy. Figure 2c shows the plan-view HR-TEM image of the Sb_2Te_3/hBN/Bi_2Se_3 heterostructure, taken near the edge of a hole in the SiN_x membrane so that there is a region where only Bi_2Se_3 is grown on hBN (first growth on the top side) without the coverage of Sb_2Te_3 (second growth on the bottom side). While the moiré patterns arise from the lattice mismatch between Sb_2Te_3 and Bi_2Se_3 (~2.8%) (refs.[28,29]) and their small in-plane misorientations (Fig. 2d), the FFT patterns of the selected areas of the image (Fig. 2d,e) identify the epitaxial alignment between Bi_2Se_3 and hBN as well as the epitaxial alignment between the Bi_2Se_3 and Sb_2Te_3 films through the hBN substrate: $\{10\bar{1}0\}_{\text{Bi}_2\text{Se}_3} \parallel \{10\bar{1}0\}_{\text{hBN}} \parallel \{10\bar{1}0\}_{\text{Sb}_2\text{Te}_3}$. The epitaxial relationship in our bidirectional MBE on suspended hBN and graphene is consistent with that of the TI thin films grown on a single surface of hBN and graphene substrates (Extended Data Fig. 3 and ref.[22,27]), suggesting that the epitaxial alignment is mainly due to the interaction with the suspended vdW substrate layer.

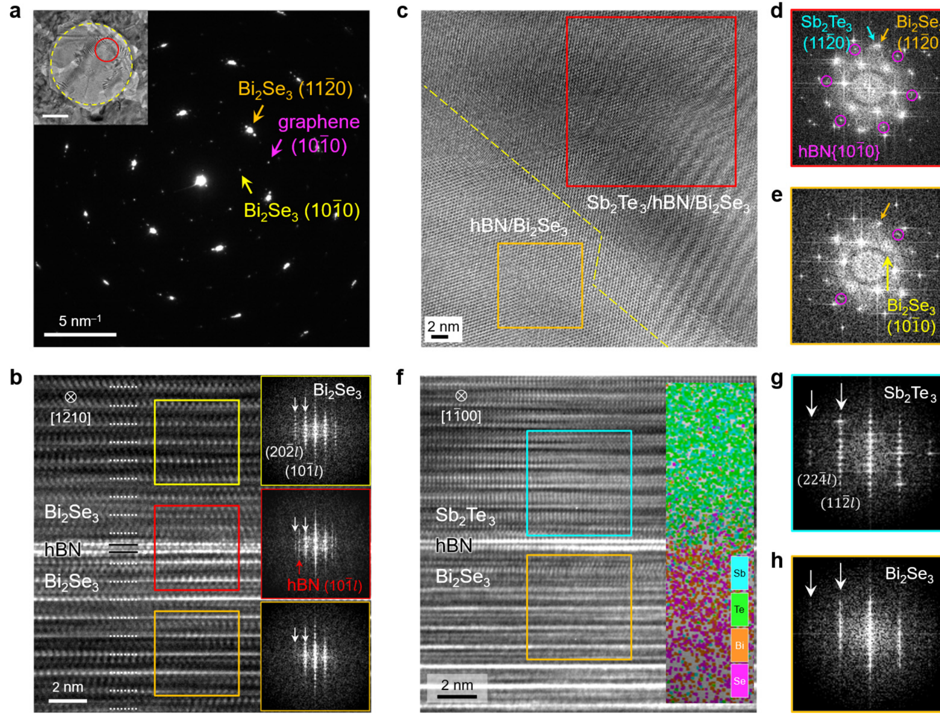

Fig. 2. Structural properties of TI/hBN(graphene)/TI double-sided vdW epitaxial heterostructures. a, Plan-view SAED pattern of Bi_2Se_3/monolayer graphene/Bi_2Se_3. Inset: Plan-view bright-field (BF) TEM image of the heterostructure. The dashed yellow circle and the red circle indicate the suspended area (a hole in the SiN_x membrane) and the area in which the SAED is recorded, respectively. Scale bar: 200 nm. **b**, Cross-sectional HR-TEM image of Bi_2Se_3/2ML hBN/Bi_2Se_3 taken along the zone axis $[1\bar{2}10]$. Insets: FFT patterns of the areas corresponding to the yellow, red, and orange boxes in the main panel. **c**, Plan-view HR-TEM image of Sb_2Te_3/few-layer hBN/Bi_2Se_3 taken around the boundary of Sb_2Te_3 (dashed yellow line). **d**,**e** FFTs of the regions marked by the red (**d**) and orange (**e**) boxes in **c**. **f**, Cross-sectional HR-TEM image of Bi_2Se_3/2ML hBN/Sb_2Te_3 taken along the zone axis $[1\bar{1}00]$. Inset: Cross-sectional STEM image overlaid with EDS map. **g**,**h** FFTs of the regions marked by cyan (**g**) and orange (**h**) boxes in **f**.

The high interfacial quality of the heterostructure is also confirmed by the cross-sectional HR-TEM (Fig. 2f). Since the strong and dense in-plane chemical bonding in the hBN layers provides a completely impermeable atomic membrane, we do not expect any interdiffusion of atoms through the hBN substrate during the growth of the second layers on the opposite side of the surface after the first layer growth. The inset of Fig. 2f shows cross-sectional chemical composition analysis using scanning tunnelling electron microscopy (STEM) equipped with energy-dispersive X-ray spectroscopy (EDS). The signals of Sb and Te are observed only above the hBN layer while those of Bi and Se are detected only below the hBN layer, demonstrating the clear spatial separation of Sb_2Te_3 and Bi_2Se_3 across the two-atom-thick hBN barrier. The epitaxial relationship across the hBN substrate can be again confirmed by comparing the FFT patterns of Bi_2Se_3 and Sb_2Te_3. As shown in Fig. 2g,h, the $(11\bar{2}l)$ and $(22\bar{4}l)$ spots of Bi_2Se_3 (white arrows in Fig. 2g) align well with the

corresponding spots of Sb_2Te_3 (white arrows in Fig. 2h).

With the hBN barrier layer, our double-sided vdW epitaxy provides TI/hBN/TI tunnelling devices, enabling the study of electron tunnelling properties of helical Dirac fermions through the tunnelling barrier. To perform tunnelling spectroscopy, individual electrical contacts to an array of suspended junctions are fabricated on the top side while they share a common bottom contact (Fig. 3a; see also Extended Data Fig. 4 and Methods). A DC bias voltage V is applied to the top electrode with respect to the bottom electrode, and the tunnelling current I can be measured across the junction. Although we have fabricated tunnelling devices on Bi_2Se_3/hBN/Bi_2Se_3 as well (results in Extended Data Fig. 5), in the remainder of this paper, we focus on the Bi_2Se_3 (bottom)/hBN/Sb_2Te_3 (top) heterostructure, whose configuration yields n-TI/insulator/p-TI junctions.

The Bi_2Se_3/hBN/Sb_2Te_3 heterojunction at zero bias is expected to form a type-III band alignment with a broken gap due to the large difference in their electron affinities and relatively small bulk band gaps (Fig. 3b)[30,31]. Accordingly, charge transfer and band bending result in carrier accumulation near the junction. Away from the heterointerface, the Fermi level E_F of Bi_2Se_3 (Sb_2Te_3) films is located near the edge of the bulk conduction (valence) band due to the unintentional n-type (p-type) doping[22,31,32]. The TSSs at the interface are hence electrically contacted by the bulk states.

Figure 3c shows $J(V)$, the current density J as a function of the applied bias voltage V, measured in devices with different hBN barriers ranging from 2 to 5 ML. The measured differential conductance at zero bias, normalized by the junction area $G_0 = \partial I/\partial V(V = 0)$, scales exponentially with the thickness of the insulating hBN barrier (inset of Fig. 3c), suggesting that electron transport in our devices is dominated by tunnelling through hBN barriers[33,34]. For a negative bias voltage, $|J(V)|$ monotonically increases rapidly with increasing $|V|$. However, for the positive bias side, $J(V)$ increases non-monotonically as V increases, exhibiting negative differential conductance-like characteristics at a certain bias voltage range. These features are consistent with the characteristics of tunnel diodes formed by p–n junctions with broken bandgap alignments[35].

The detailed tunnelling process in the junction can be described in the differential conductance $G(V) = \partial I/\partial V$ curve for the device with a 2 ML hBN barrier (Fig. 3d). Schematic band alignments at the heterointerface under different bias voltages are illustrated together, as labeled by (i) – (iv). The differential conductance exhibits a strongly reduced value between bias voltage regions (i) and (iv), indicating that the Fermi level of n-Bi_2Se_3 (E_F^{BS})

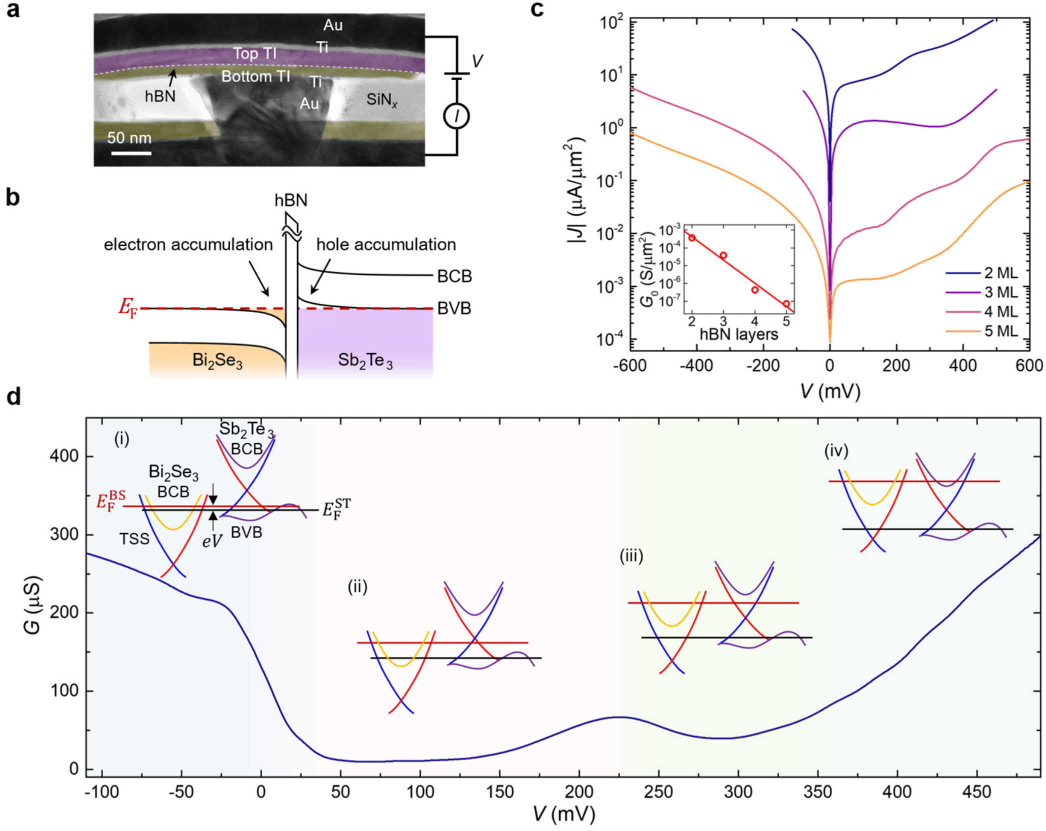

Fig. 3. Tunnelling spectroscopy in Bi_2Se_3/hBN/Sb_2Te_3 junctions at zero magnetic field. **a**, False-coloured low-magnification cross-sectional BF TEM image of a vertical tunnel junction device in two-terminal measurement configuration. While this image shows Bi_2Se_3/hBN/Bi_2Se_3, the device structure is identical for all measured junctions, including Bi_2Se_3/hBN/Sb_2Te_3, except for the hBN barrier thickness and the junction area. **b**, Schematic band alignment of the Bi_2Se_3/hBN/Sb_2Te_3 junction at zero bias voltage, depicted in energy – out-of-plane axis plane. **c**, Tunnelling current density as a function of bias voltage for the devices with different thicknesses of hBN barrier. V is applied to Sb_2Te_3 (top), and the current drained through Bi_2Se_3 (bottom), I, is measured. Inset: Zero-bias differential conductance per unit area as a function of the number of hBN layers. **d**, Differential conductance of the Bi_2Se_3/2ML hBN/Sb_2Te_3 device as a function of V. (i) – (iv): Schematic band alignments at the tunnelling interface under different bias conditions, plotted in the energy – in-plane momentum plane. TSSs are marked by red and blue colours, indicating their spin-momentum locking textures. The tunnelling conductance is determined by the position of the bulk conduction band (BCB) and the bulk valence band (BVB) relative to the $E_{\mathrm{F}}^{\mathrm{BS}}$ and $E_{\mathrm{F}}^{\mathrm{ST}}$. Devices with 2 and 3 ML hBN barriers are measured at temperature T = 1.8 K and those with 4 ML and 5 ML barriers are measured at T = 1.5 K.

crosses the bulk band gap of p-Sb_2Te_3 as V is increased in this region. As the Fermi level of p-Sb_2Te_3 ($E_{\mathrm{F}}^{\mathrm{ST}}$) moves out of the BCB of n-Bi_2Se_3 and into its bulk band gap ((ii) and (iii)), the $G(V)$ exhibits a peak at V = 225 mV. This local maximum can be attributed to the enhanced tunnelling density of states (DOS) when the bulk band edges align in the presence of band bending[36-38]. At $V \lesssim$ 40 mV and $V \gtrsim$ 350 mV, oscillatory spectral features appear due to the bulk quantum well states (QWSs)[38-40].

The topological nature of the coupled surface states in our vdW epitaxial structure can be revealed by the magneto-tunneling transport study. When magnetic field perpendicular to the junction, $B_\perp$, is applied, LLs form in the TSSs, which can modulate the tunnel conductance associated with the TSSs[40-43]. Figure 4a shows the differential conductance spectra $G(V, B_\perp) = \partial I/\partial V(V, B_\perp)$ of the Sb_2Te_3/2ML hBN/Bi_2Se_3 device at different $B_\perp$. As $B_\perp$ increases, the tunnelling conductance spectrum exhibits additional oscillatory features. A more systematic analysis can be performed by subtracting off the zero magnetic field conductance: $\Delta G(V, B_\perp) = \partial I/\partial V(V, B_\perp) - \partial I/\partial V(V, B_\perp = 0)$. Figure 4b shows ΔG as a function of V and $B_\perp$. We observe that $\Delta G(V)$ oscillations exhibit larger amplitudes at higher $B_\perp$. These oscillatory features can be categorized into three groups: oscillations with peak and valley positions (I) that are independent of $B_\perp$; (II) that vary with $B_\perp$ and converges to V ~135 mV as $B_\perp$ vanishes; and (III) that vary with $B_\perp$ and converges to a large bias voltage (V > 450 mV) as we extrapolate the position of the origin.

To further investigate the nature of ΔG oscillation, we tilt the magnetic field, B, and provide a component of the magnetic field parallel to the junction, $B_{/\!/}$. Figure 4b–e shows $\Delta G(V, B)$ at different $B_\perp$ and $B_{/\!/}$. We find that the oscillatory feature (I) depends only on the total magnetic field B, indicating a 3D isotropic nature, while features (II) and (III) depend only on $B_\perp$, suggesting a 2D origin. We attribute the feature (I) to the bulk QWSs due to its angle-insensitivity and the bias voltage ranges in which the peaks appear (see Extended Data Fig. 6).

The 2D oscillatory features (II) and (III) can be related to the resonant tunnelling associated with LL formation in the TSSs. In particular, the observed unequal spacing, which increases with increasing $B_\perp$, suggests that these LLs originate from the linearly dispersed Dirac spectrum of the TSSs. In a perpendicular magnetic field, the Dirac dispersion of the TSSs can lead to sharply quantized LLs at energy $E_n = E_D + \mathrm{sgn}(n) v_\mathrm{F} \sqrt{2e\hbar|n|B_\perp}$, where E_D is the energy of Dirac point (DP), v_F is the Fermi velocity of the TSSs, e is the elementary charge, $\hbar$ is the reduced Planck constant, and $n = 0, \pm 1, \pm 2, \ldots$ is the LL index, ignoring the Zeeman energy[40-43]. As the bias voltage increases, V > 20 mV, the resonant tunnelling between the BCB of Bi_2Se_3 and the LLs developed in the TSS of Sb_2Te_3 becomes possible, and indeed, the oscillatory features (II) in the magneto-tunnelling spectra Fig. 4b–d follow $e(V - V_0) = \mathrm{sgn}(n) v_\mathrm{F} \sqrt{2e\hbar|n|B_\perp}$, centered around $V_0 \approx 135$ mV. We identify the peaks of these oscillations, V_n, and assign the LL indices n as shown in the upper part of Fig. 4b, marked by grey fonts (see Extended Data Fig. 7). We then plot the positions of the peaks in energy eV_n against

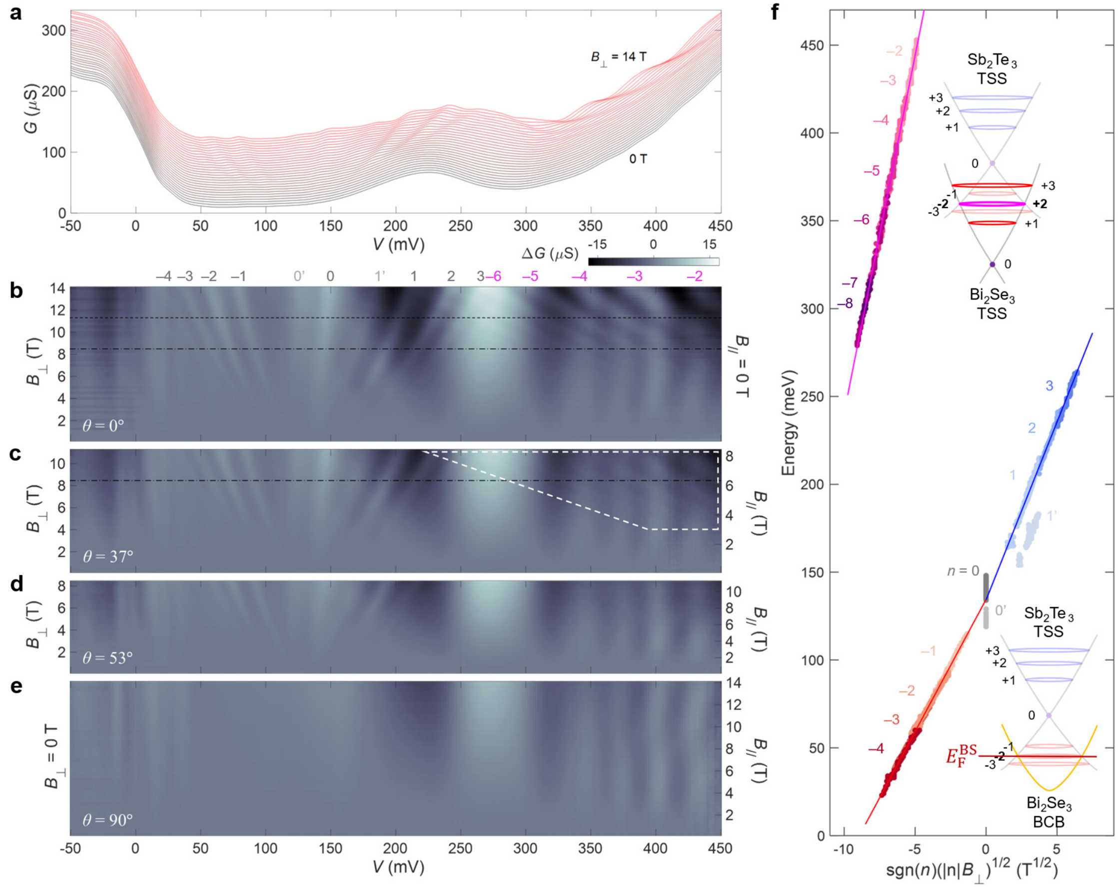

Fig. 4. Magnetic field-dependent tunnelling conductance of the Bi_2Se_3/2ML hBN/Sb_2Te_3 device. a, $B_\perp$-dependence of tunnelling conductance. Spectra under different fields, in 0.5 T increments, are vertically offset by 4 μS for clarity. **b**–**e**, Colour scale maps showing the field-modulated component of the conductance $\Delta G(V, B)$ at different field angles θ defined with respect to the out-of-plane direction. Perpendicular and in-plane components of the field are indicated by the left and right ticks, respectively. Vertical axes of **b**–**d** are adjusted to have the same $B_\perp$ scale, while those of **b**,**e** have the same $|B|$ scale. The black dashed (dash-dotted) horizontal line indicates the maximum $B_\perp$ in **c** (**d**). **f**, LL peak positions at different $B_\perp$ plotted versus $\mathrm{sgn}(n)(|n|B_\perp)^{1/2}$. The lines are linear fits to the data. The lower (upper) inset is the schematic representation of the band alignment that causes the LL peaks in the tunnelling conductance to appear at lower (higher) bias voltages. The spin helicity of the TSSs is expressed in red and blue colours. Numbers denote LL indices. All measurements are performed at $T = 1.8$ K.

$\mathrm{sgn}(n)\sqrt{|n|B_\perp}$ as shown in the lower part of Fig. 4f. Remarkably, all data points for $n > 0$ (electron LLs) and $n < 0$ (hole LLs) separately form a straight line and converge at $B_\perp = 0$ when extrapolated, within 1 mV which is our measurement resolution. The slope of each linear fit line provides the estimation of the v_F of the corresponding TSS: we obtain $v_F \approx 4.1 \times 10^5$ m/s for $n < 0$ LLs (red line) and 5.6×10^5 m/s for $n > 0$ LLs (blue line), and the corresponding bands are assigned to the valence and conduction band of TSSs in Sb_2Te_3, respectively.

There are, however, two exceptional data sets that do not fall into the LL schemes discussed above. First, the peak of the oscillation corresponding to $n = 0$, started at $V_0 \approx 135$

mV at zero magnetic field, exhibits a weak linear dispersion as $B_\perp$ increases, with an estimated g-factor of ~29. Applying an external magnetic field to the TSS breaks the time-reversal symmetry to open a gap, causing a Zeeman energy shift, most significantly affecting the zeroth LL[44]. The experimentally measured g-factors, however, vary widely among the experiments[43-45]. Second, there exists another copy of n = 0 and 1 LL peaks, marked as 0' and 1' respectively, emerging at lower bias voltages with smaller intensities. Although their origin is unclear, these modulations do not split from or merge with the main LL peaks.

We now turn our attention to the high bias oscillations (III) above. We identify their peak positions V_n^* and assign the corresponding LL indices (Extended Data Fig. 4), marked by magenta fonts in the upper part of Fig. 4b. We then perform a similar analysis as for (II) and obtain the corresponding LL origin $V_0^* \approx 647$ mV and velocity $v \approx 1.1 \times 10^6$ m/s (magenta line in Fig. 4f). At this higher bias voltage regime, both of the $E_{\mathrm{F}}^{\mathrm{BS}}$ and $E_{\mathrm{F}}^{\mathrm{ST}}$ are outside of the BVB and BCB of the counterpart, respectively, and the resonant tunnelling can occur between the LLs developed in the TSSs of Bi_2Se_3 and Sb_2Te_3 (see the upper inset schematic in Fig. 4f). In order for such tunnelling to happen, the quantized energy, E_n, and angular momentum of LLs, $k_n = \sqrt{2e|n|B_\perp/\hbar}$, as well as the spin-momentum locking helicity of TSSs should be matched. Considering the two TSSs at the tunnelling interface have the opposite spin-momentum locking helicity due to their opposite surface normal directions, the only allowed inter-LL resonant tunnelling is the inter-band tunnelling between an occupied – n^{th} LL of Bi_2Se_3 to an unoccupied n^{th} LL of Si_2Te_3 satisfying $eV_n^* + E_{\mathrm{D}}^{\mathrm{BS}} - \mathrm{sgn}(n)v_{\mathrm{F}}^{\mathrm{BS}}\sqrt{2e\hbar|n|B_\perp} = E_{\mathrm{D}}^{\mathrm{ST}} + \mathrm{sgn}(n)v_{\mathrm{F}}^{\mathrm{ST}}\sqrt{2e\hbar|n|B_\perp}$, where $v_{\mathrm{F}}^{\mathrm{BS(ST)}}$ and $E_{\mathrm{D}}^{\mathrm{BS(ST)}}$ are the Fermi velocity and the DP energy of the Bi_2Se_3 (Sb_2Te_3) TSS measured with respect to the $E_{\mathrm{F}}^{\mathrm{BS(ST)}}$, respectively. This relationship results in a straight line in the plot of eV_n^* versus $\mathrm{sgn}(n)\sqrt{|n|B_\perp}$ as shown in the upper part of Fig. 4f, where the slope of this line corresponds to $v_{\mathrm{F}}^{\mathrm{BS}} + v_{\mathrm{F}}^{\mathrm{ST}}$, which is approximately twice as high as v_F for TSSs Bi_2Se_3 and of Sb_2Te_3[32,40,41,43,46], in agreement with our observation. Thus, the energy-momentum-spin resonance between two sets of LLs manifests as the sum of the v_{F}'s of Bi_2Se_3 and Sb_2Te_3.

Finally, we discuss the effect of the in-plane magnetic field $B_{/\!/}$ on the resonant tunnelling between LLs. As shown in Fig. 4c,d, the ΔG peaks corresponding to inter-LL tunnelling (III) are rapidly suppressed with increasing $B_{/\!/}$ (e.g., compare the LL peaks in the region highlighted by the white dashed box in Fig. 4c with the corresponding $B_\perp$ and V ranges in Fig. 4b,d). The application of $B_{/\!/}$ provides an in-plane momentum gain to the tunnelling

electrons[6,8], which suppresses inter-band inter-LL resonant tunnelling, where the energy, angular momentum, and spin of the electrons must be conserved. Note that the tunnelling from bulk band to LL (II) is not suppressed by the presence of finite $B_{//}$ (Fig. 4b–d), since the electron momentum is not quantized in the BCB of Bi_2Se_3 from which electrons tunnel.

The realization of two different types of TI materials epitaxially coupled via an ultrathin crystalline barrier, with atomically sharp and clean interfaces and without chemical intermixing, has allowed us to systematically investigate the selection rules of electron tunnelling between the TSSs. Our results show that the two TSSs can be brought together to a sub-nm distance, which is much shorter than the thickness limit of a single 3D TI slab thanks to the wide bandgap of hBN[39,40,47,48]. This system can serve as a platform to explore interesting physics involving coupled TSSs, such as the proposed topological exciton condensation[14,15]. The double-sided vdW epitaxial growth technique can be further applied to various combinations of vdW materials including superconductors and ferromagnets, potentially leading to emergent phenomena and novel device applications.

References

1. Geim, A. K. & Grigorieva, I. V. Van der Waals heterostructures. *Nature* **499**, 419-425 (2013).
2. Novoselov, K. S., Mishchenko, A., Carvalho, A. & Castro Neto, A. H. 2D materials and van der Waals heterostructures. *Science* **353**, aac9439 (2016).
3. Bretheau, L. *et al.* Tunnelling spectroscopy of Andreev states in graphene. *Nat. Phys.* **13**, 756-760 (2017).
4. Jung, S. *et al.* Direct probing of the electronic structures of single-layer and bilayer graphene with a hexagonal boron nitride tunneling barrier. *Nano Lett.* **17**, 206-213 (2017).
5. Song, T. *et al.* Giant tunneling magnetoresistance in spin-filter van der Waals heterostructures. *Science* **360**, 1214-1218 (2018).
6. Mishchenko, A. *et al.* Twist-controlled resonant tunnelling in graphene/boron nitride/graphene heterostructures. *Nat. Nanotechnol.* **9**, 808-813 (2014).
7. Greenaway, M. T. *et al.* Resonant tunnelling between the chiral Landau states of twisted graphene lattices. *Nat. Phys.* **11**, 1057-1062 (2015).
8. Wallbank, J. R. *et al.* Tuning the valley and chiral quantum state of Dirac electrons in van der Waals heterostructures. *Science* **353**, 575-579 (2016).
9. Heremans, J. P., Cava, R. J. & Samarth, N. Tetradymites as thermoelectrics and topological insulators. *Nat. Rev. Mater.* **2**, 17049 (2017).
10. Shibayev, P. P. *et al.* Engineering topological superlattices and phase diagrams. *Nano Lett.* **19**, 716-721 (2019).
11. Zhao, Y.-F. *et al.* Tuning the Chern number in quantum anomalous Hall insulators. *Nature* **588**, 419-423 (2020).
12. Deng, P. *et al.* Topological surface state annihilation and creation in SnTe/$Cr_x(BiSb)_{2-x}Te_3$ heterostructures. *Nano Lett.* **22**, 5735-5741 (2022).
13. Kou, L. *et al.* Graphene-based topological insulator with an intrinsic bulk band gap above room temperature. *Nano Lett.* **13**, 6251-6255 (2013).
14. Seradjeh, B., Moore, J. E. & Franz, M. Exciton condensation and charge fractionalization in a topological Insulator film. *Phys. Rev. Lett.* **103**, 066402 (2009).
15. Wang, Z., Hao, N., Fu, Z.-G. & Zhang, P. Excitonic condensation for the surface states of topological insulator bilayers. *New J. Phys.* **14**, 063010 (2012).
16. Wang, Z. Y. *et al.* Superlattices of Bi_2Se_3/In_2Se_3: Growth characteristics and structural properties. *Appl. Phys. Lett.* **99**, 023112 (2011).
17. Kim, Y. *et al.* Remote epitaxy through graphene enables two-dimensional material-based layer transfer. *Nature* **544**, 340-343 (2017).
18. Kong, W. *et al.* Polarity governs atomic interaction through two-dimensional materials. *Nat. Mater.* **17**, 999-1004 (2018).
19. Hong, Y. J. *et al.* Van der Waals Epitaxial Double Heterostructure: InAs/Single-Layer Graphene/InAs. *Adv. Mater.* **25**, 6847-6853 (2013).
20. Tchoe, Y. *et al.* Vertical monolithic integration of wide- and narrow-bandgap semiconductor nanostructures on graphene films. *NPG Asia Mater.* **13**, 33 (2021).
21. Tsen, A. W. *et al.* Tailoring electrical transport across grain boundaries in polycrystalline graphene. *Science* **336**, 1143-1146 (2012).
22. Park, J. Y. *et al.* Molecular beam epitaxial growth and electronic transport properties of high quality topological insulator Bi_2Se_3 thin films on hexagonal boron nitride. *2D Mater.* **3**, 035029 (2016).
23. Lapano, J. *et al.* Van der Waals epitaxy growth of Bi_2Se_3 on a freestanding monolayer graphene membrane: Implications for layered materials and heterostructures. *ACS Appl. Nano Mater.* **4**, 7607-7613 (2021).
24. Ko, K. *et al.* Operando electron microscopy investigation of polar domain dynamics in twisted van der Waals homobilayers. *Nat. Mater.* **22**, 992-998 (2023).

25. Liu, Y. *et al.* Tuning Dirac states by strain in the topological insulator Bi_2Se_3. *Nat. Phys.* **10**, Advanced Materials294-299 (2014).
26. Park, J. Y. *et al.* Bi_2Se_3 thin films heteroepitaxially grown on α−$RuCl_3$. *Phys. Rev. Mater.* **4**, 113404 (2020).
27. Guha, P. *et al.* Molecular beam epitaxial growth of Sb_2Te_3–Bi_2Te_3 lateral heterostructures. *2D Mater.* **9**, 025006 (2022).
28. Nakajima, S. The crystal structure of $Bi_2Te_{3-x}Se_x$. *J. Phys. Chem. Solids* **24**, 479-485 (1963).
29. Anderson, T. L. & Krause, H. B. Refinement of the Sb_2Te_3 and Sb_2Te_2Se structures and their relationship to nonstoichiometric $Sb_2Te_{3-y}Se_y$ compounds. *Acta Cryst. B* **30**, 1307-1310 (1974).
30. Takane, D. *et al.* Work function of bulk-insulating topological insulator $Bi_{2-x}Sb_xTe_{3-y}Se_y$. *Appl. Phys. Lett.* **109**, 091601 (2016).
31. Levy, I. *et al.* Designer topological insulator with enhanced gap and suppressed bulk conduction in Bi_2Se_3/Sb_2Te_3 ultrashort-period superlattices. *Nano Lett.* **20**, 3420-3426 (2020).
32. Zhang, J. *et al.* Band structure engineering in $(Bi_{1-x}Sb_x)_2Te_3$ ternary topological insulators. *Nat. Commun.* **2**, 574 (2011).
33. Britnell, L. *et al.* Electron tunneling through ultrathin boron nitride crystalline barriers. *Nano Lett.* **12**, 1707-1710 (2012).
34. Chandni, U., Watanabe, K., Taniguchi, T. & Eisenstein, J. P. Evidence for defect-mediated tunneling in hexagonal boron nitride-based junctions. *Nano Lett.* **15**, 7329-7333 (2015).
35. Yan, R. *et al.* Esaki diodes in van der Waals heterojunctions with broken-gap energy band alignment. *Nano Lett.* **15**, 5791-5798 (2015).
36. Cappelluti, E., Grimaldi, C. & Marsiglio, F. Topological change of the Fermi surface in low-density Rashba gases: application to superconductivity. *Phys. Rev. Lett.* **98**, 167002 (2007).
37. Sun, Y. J. *et al.* Van Hove singularities as a result of quantum confinement: The origin of intriguing physical properties in Pb thin films. *Nano Res.* **3**, 800-806 (2010).
38. Bahramy, M. S. *et al.* Emergent quantum confinement at topological insulator surfaces. *Nat. Commun.* **3**, 1159 (2012).
39. Zhang, Y. *et al.* Crossover of the three-dimensional topological insulator Bi_2Se_3 to the two-dimensional limit. *Nat. Phys.* **6**, 584-588 (2010).
40. Jiang, Y. *et al.* Landau quantization and the thickness limit of topological insulator thin films of Sb_2Te_3. *Phys. Rev. Lett.* **108**, 016401 (2012).
41. Cheng, P. *et al.* Landau quantization of topological surface states in Bi_2Se_3. *Phys. Rev. Lett.* **105**, 076801 (2010).
42. Hanaguri, T., Igarashi, K., Kawamura, M., Takagi, H. & Sasagawa, T. Momentum-resolved Landau-level spectroscopy of Dirac surface state in Bi_2Se_3. *Phys. Rev. B* **82**, 081305 (2010).
43. Yoshimi, R. *et al.* Dirac electron states formed at the heterointerface between a topological insulator and a conventional semiconductor. *Nat. Mater.* **13**, 253-257 (2014).
44. Fu, Y.-S. *et al.* Observation of Zeeman effect in topological surface state with distinct material dependence. *Nat. Commun.* **7**, 10829 (2016).
45. Zhang, Z. *et al.* Zeeman effect of the topological surface states revealed by quantum oscillations up to 91 Tesla. *Phys. Rev. B* **92**, 235402 (2015).
46. Xia, Y. *et al.* Observation of a large-gap topological-insulator class with a single Dirac cone on the surface. *Nat. Phys.* **5**, 398-402 (2009).
47. Jin, H., Im, J., Song, J.-H. & Freeman, A. J. Multiple Dirac fermions from a topological insulator and graphene superlattice. *Phys. Rev. B* **85**, 045307 (2012).
48. Costa, M. *et al.* Controlling topological states in topological/normal insulator heterostructures. *ACS Omega* **3**, 15900-15906 (2018).

Methods

Preparation of suspended ultrathin hBN and graphene

For vertical tunnel junctions, atomically thin hBN single crystal flakes are prepared by mechanical exfoliation on the oxygen-plasma treated surfaces of Si substrates with a 90 nm SiO_2 layer and identified by optical microscopy. The thickness and surface cleanliness of the identified layers are further characterized by AFM. We choose 2–5 ML hBN for the tunnel barrier because they provide reliably working tunnel junctions over a suitable current and bias voltage range. The target flake is then picked up and transferred onto perforated SiN_x membranes using sticky polymer films, such as polycaprolactone (PCL)[49] or polycarbonate (PC), on polydimethylsiloxane (PDMS) stamps. Here, we employ 50 nm thick low-stress silicon-rich nitride membranes with TEM-compatible silicon frames (Silson Ltd). Arrays of holes with typical diameters of 0.4 – 1 μm are fabricated in the SiN_x membranes by standard electron (*e*)-beam lithography and CF_4/Ar reactive ion etching. The oxygen plasma treatment of the SiN_x membranes immediately prior to the drop-down process enhances the adhesion between the vdW layers and the membranes, reducing the risk of wash-away of the flake or wrinkles formation during the subsequent wet process. After the transfer, the sticky polymer is removed by organic solvents: tetrahydrofuran (THF) for PCL and chloroform for PC. Finally, the sample is annealed (typically at 350–400ºC) under high vacuum to reduce the polymer residues. For plan-view TEM study of the double-sided vdW epitaxial heterostructures, we also employ few-layer hBN epitaxially grown on a sapphire substrate[50] and monolayer graphene grown on a Cu foil. These CVD-grown large-scale vdW substrate layers are suspended on the holey SiN_x membranes by the poly(methyl methacrylate) (PMMA)-assisted wet transfer method. The suspended vdW layer undergoes another round of *in-situ* thermal cleaning in the UHV-MBE chamber before the growth of TI thin films.

Double-sided vdW-MBE growth

First, unless otherwise stated, Bi_2Se_3 thin films are typically grown first on the bottom surface of the suspended hBN or graphene through the holes in the SiN_x membranes by loading the chip upside-down on a substrate holder of the MBE. We employ the two-step growth process developed for high-quality Bi_2Se_3 thin film growth on vdW-layered substrates[22,26]. The top surface of the suspended vdW layer remains intact after bottom side growth, preserving its atomically clean surface (see Fig. 1h). This growth result is attributed to the highly directional molecular fluxes of the precursors which are hardly subject to scattering events during MBE

growth in a UHV environment. Next, the substrate is inverted *ex-situ* and loaded back to the MBE chamber so that the top side faces the molecular fluxes. Another round of two-step MBE growth is then performed to grow either Bi_2Se_3 or Sb_2Te_3 thin films on top of the hBN(graphene)/Bi_2Se_3 heterostructure using a similar two-step growth process[27]. In this step, care is taken to protect the pre-grown Bi_2Se_3 such as omitting the thermal cleaning process and reducing the 2nd step growth temperature. The b-TI film has crystalline structures up to the interface with hBN and exhibits similar structural quality to the t-TI film (Fig. 2b,f), indicating that the hBN layer provides excellent protection of the bottom layer from the environment during the *ex-situ* sample flipping process and subsequent growth of the top layer. The typical thickness of the TI films is 20 QL for the top side and 10 QL for the bottom side.

Microstructural characterizations

The TEM lamella for the cross-sectional study is prepared by a focused ion beam system (FEI Helios 650). Field-emission TEMs with an acceleration voltage of 200 kV (JEOL JEM-2100F and FEI Tecnai F20) are used for HR imaging. An average background subtraction filter is applied to remove noise in the HR-TEM images. The elemental distribution mapping is performed with a silicon drift detector-based EDS system operating in the STEM mode and analyzed with AZtec software (Oxford Instruments).

Device fabrications

Electrical contacts on both sides of the suspended TI/hBN/TI heterostructures, prepared on SiN_x membrane templates, are fabricated by the following steps. First, Ti/Au 5/200 nm metal layer is deposited on the bottom side of the sample by *e*-beam evaporation. The thick metal layer provides ohmic contacts to the bottom TI and mechanical support to the membrane for the following fabrication steps. We note that the frames of our membrane chips are made of high-resistivity silicon, which becomes insulating at low temperatures. The individual top ohmic contacts to the array of junctions are fabricated by *e*-beam lithography followed by *e*-beam evaporation of Ti/Au 5/55 nm. Using the metal contacts as etch masks, an Ar plasma etching is carried out to remove the TI films on the uncovered area, electrically separating the array of junctions. Finally, bonding pads and interconnection lines to the contacts are deposited by another round of *e*-beam lithography and *e*-beam evaporation of Ti/Pd/Au 5/20/125 nm. The typical junction area is in the range of 0.2 to 0.7 μm^2.

Magneto-tunnelling measurements

The current–voltage characteristics of the tunnelling devices are measured using a voltage source (Yokogawa GS200 DC voltage source or Keithley Instruments 2400 SourceMeter) to apply DC bias voltage and a low-noise current preamplifier (DL Instruments Model 1211) connected to a digital multimeter (Agilent 34401A) for measuring the current. The differential conductance is measured simultaneously with the current–voltage curve by mixing the DC bias voltage with a small AC excitation voltage of 2 mV at 47.77 Hz using a lock-in amplifier (SR830, Stanford Research Systems), a voltage divider, and a transformer. Temperature and magnetic field are controlled by either Oxford Instruments Teslatron PT (base temperature T_{base} = 1.5 K, maximum magnetic field B_{max} = 8 T) or Quantum Design Physical Property Measurement System (T_{base} = 1.8 K, B_{max} = 14 T). The angle of magnetic fields with respect to the tunnelling interface is controlled by changing the orientation of sample *ex-situ*. For each field angle, tunnelling characteristics at zero magnetic field are cross-checked to confirm the robustness of the tunnelling conductance against thermal cycling. The Bi_2Se_3/hBN/Bi_2Se_3 device presented in Extended Data Fig. 5 is measured at the National High Magnetic Field Laboratory (T_{base} = 0.3 K, B_{max} = 31.5 T) with a rotator probe that can change the orientation of sample *in-situ*. During the device fabrication, loading, and shipping processes, meticulous measures are implemented to prevent electrostatic discharge.

Data availability

The data that support the findings of this study are presented in the Article and its Extended Data. Further data are available from the corresponding authors upon reasonable request.

References

49. Son, S. *et al.* Strongly adhesive dry transfer technique for van der Waals heterostructure. *2D Mater.* **7**, 041005 (2020).
50. Jang, A. R. *et al.* Wafer-scale and wrinkle-free epitaxial growth of single-orientated multilayer hexagonal boron nitride on sapphire. *Nano Lett.* **16**, 3360-3366 (2016).

Acknowledgements

We thank J. Eom, Y. S. Kim, and C.-H. Lee for their help in the transfer of atomically thin vdW crystals on the perforated SiN_x membranes. The major part of this work was supported by the Office of Naval Research (ONR) Multidisciplinary University Research Initiatives (MURI)

program (N00014-21-1-2377) and the Science Research Center (SRC) for Novel Epitaxial Quantum Architectures (NRF-2021R1A5A1032996). J.S., J. K., and D.K. acknowledge support from the National Research Foundation of Korea (NRF) grants funded by the Korean Government (MSIT) (RS-2023-00283291, RS-2023-00207732, and No. 2023R1A2C2005809). J.J. and M.K. acknowledge support from the NRF grant NRF-2022R1A2C3007807. H.S.S acknowledges support from the Institute for Basic Science (IBS-R036-D1). A portion of the user collaboration grant program (UCGP) project was performed at the National High Magnetic Field Laboratory supported by the National Science Foundation through NSF/DMR-1644779 and the State of Florida. K.W. and T.T. acknowledge support from the JSPS KAKENHI (Grant Numbers 20H00354 and 23H02052) and World Premier International Research Center Initiative (WPI), MEXT, Japan.

Author contributions

P.K., G.-C.Y., and J.Y.P. conceived the experiments. J.Y.P. performed the double-sided vdW epitaxy and fabricated the tunnelling devices. J.Y.P. and G.-C.Y. analysed and optimized these processes. J.Y.P. performed the magneto-tunnelling measurements together with J.S. and J.K.. J.Y.P., R.M.H., A.G., and W.K.P. carried out the measurement at the National High Magnetic Field Laboratory. J.Y.P., J.S., J.K., D.K., and P.K. analysed the transport data. J.J. conducted the TEM experiments. J.J., J.Y.P., G.-C.Y., and M.K. analysed the TEM data. J.Y.P. and H.Y. prepared the hole-patterned SiN_x membrane templates. Y.J.S., D.H.N., H.Y., and J.Y.P. carried out the suspension of ultrathin vdW layers on the perforated SiN_x membranes. C. H. and H.S.S. provided the epitaxial few-layer hBN films and collaborated on discussions about the double-sided vdW epitaxy on them. J.Y. grew the monolayer graphene. K.W. and T.T. provided the bulk hBN single crystals. G.-C.Y. and P.K. jointly supervised the project. J.Y.P. and P.K. wrote the manuscript with input from all authors.

Competing interests

The authors declare no competing interests.

Extended data figures

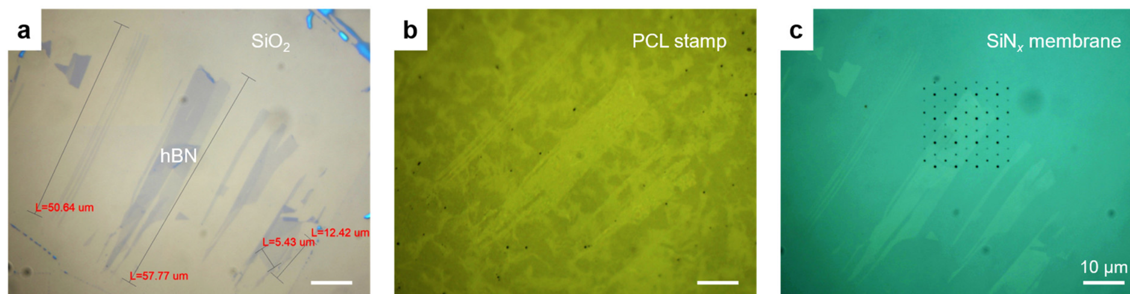

Extended Data Fig. 1. Suspension of atomically thin hBN crystals on the perforated SiN_x membrane. a–c, Optical microscope images of ultrathin hBN layers: as exfoliated on the SiO_2 surface (**a**), picked up by the PCL polymer stamp (**b**), transferred on the SiN_x membrane with premade holes (**c**).

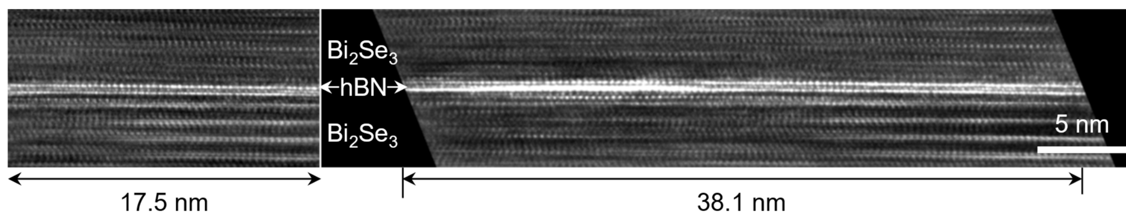

Extended Data Fig. 2. Larger scale homogeneity of the Bi_2Se_3/hBN/Bi_2Se_3 interface. Cross-sectional HR-TEM images of Bi_2Se_3/2ML hBN/Bi_2Se_3 taken along the zone axis $[1\bar{2}10]$ exhibiting atomically sharp and clean interfaces.

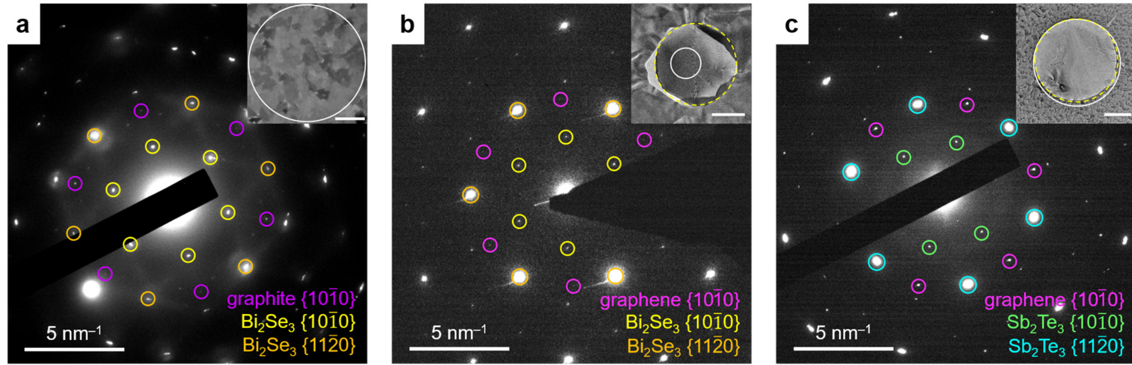

Extended Data Fig. 3. Epitaxial relationship of the TI thin films grown on a single surface of suspended graphene substrates. a–**c**, Plan-view SAED patterns of the Bi_2Se_3 thin film grown on the top surface of suspended graphite (**a**), the Bi_2Se_3 thin film grown on the bottom surface of suspended monolayer graphene (**b**), and the Sb_2Te_3 thin film grown on the top surface of suspended monolayer graphene (**c**). Insets: Plan-view TEM BF images. The white solid circles and the yellow dashed circles indicate the areas in which the SAED in the corresponding main panels are taken and the suspended regions, respectively. The entire area displayed in the inset is suspended for **a**. Scale bars in the insets: 1 μm (**a**), 200 nm (**b**), and 200 nm (**c**). All data (**a**–**c**) exhibit the preferential epitaxial relationship of $\{10\bar{1}0\}_{\mathrm{Bi_2Se_3\ or\ Sb_2Te_3}} \parallel \{10\bar{1}0\}_{\mathrm{graphene\ or\ graphite}}$, indicating that the epitaxial alignment in the double-sided vdW epitaxy is owing to the local interaction at the interface with the suspended vdW substrate layer.

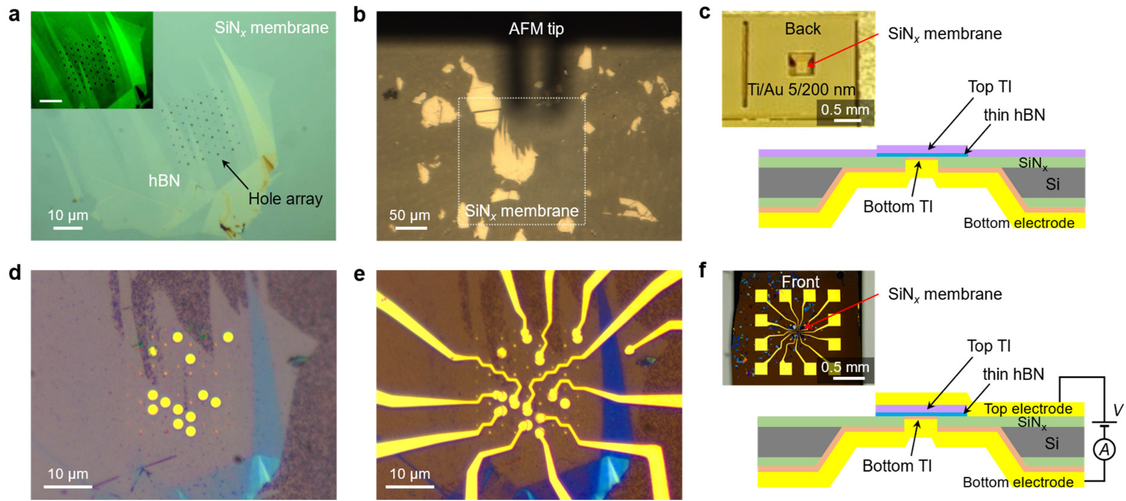

Extended Data Fig. 4. Tunneling device fabrication processes. **a**, Optical microscope image of atomically thin hBN layers suspended on the perforated SiN_x membrane. Inset: High-contrast image of the main panel. Scale bar: 10 μm. **b**, Optical microscope image of the sample in (**a**) after the double-sided vdW epitaxy of TI thin films (10 QL Bi_2Se_3 on the back side and 20 QL Sb_2Te_3 on the top side). **c**, Photograph (upper left) and schematic (lower right) of the double-sided vdW-epitaxial heterojunction after the evaporation of the Ti/Au 5/200 nm common bottom contact. **d**,**e**, Optical microscope images of the junction arrays: after the fabrication of Ti/Au 5/55 nm individual top contacts followed by Ar plasma etching (**d**) and after the formation of bonding pads and leads (Ti/Pd/Au 5/20/125 nm). **f**, Optical microscope image (upper left) and schematic structure (lower right) of the finished device.

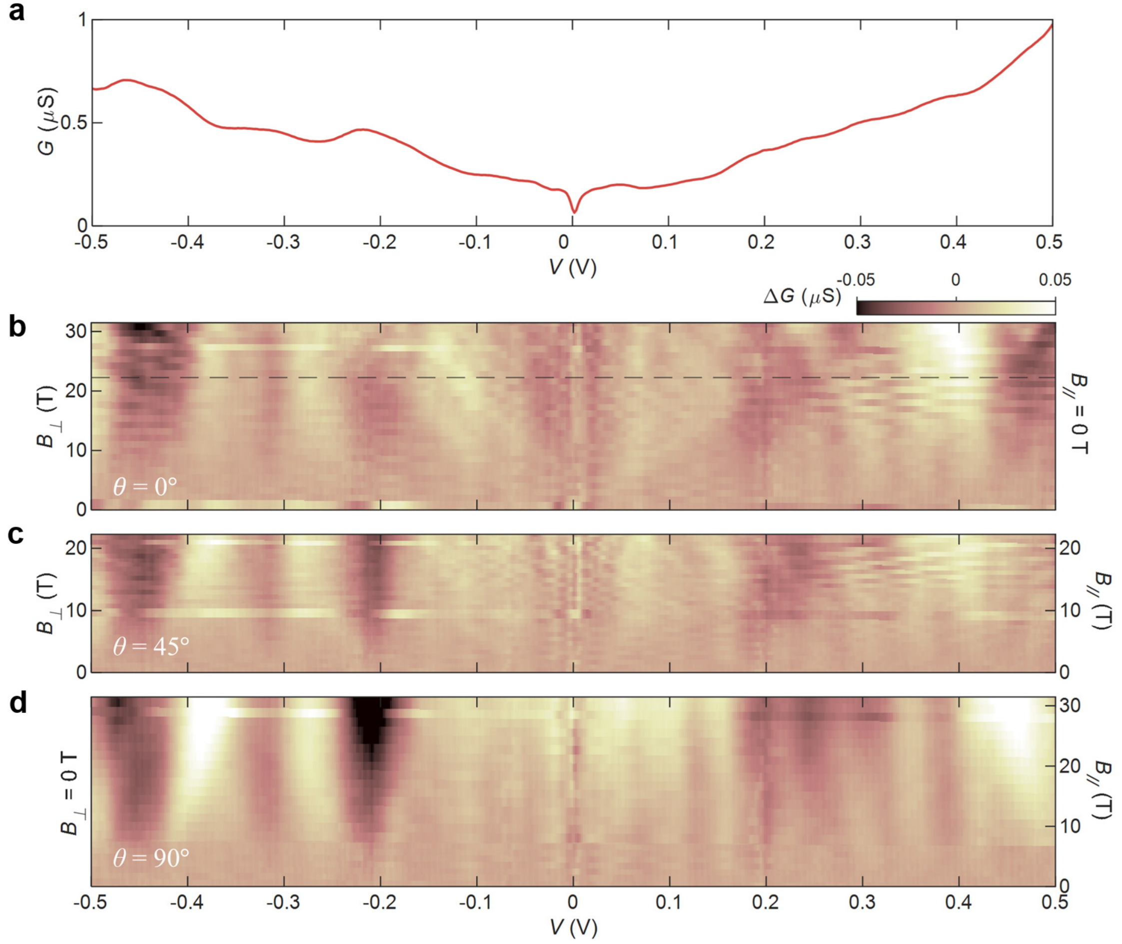

Extended Data Fig. 5. Magnetic field-dependent tunnelling conductance of a Bi_2Se_3/3 ML hBN/Bi_2Se_3 device. **a**, Differential conductance $G(V) = \partial I/\partial V$ of the Bi_2Se_3/3ML hBN/Bi_2Se_3 device at zero magnetic field. **b**–**d**, Colour scale maps showing the field-modulated component of the conductance $\Delta G(V, B)$ at different field angles: out-of-plane (**b**), 45° tilted (**c**), and in-plane (**d**) directions. $B_\perp$ and $B_{/\!/}$ components of the field are indicated by the left and right ticks, respectively. The black dashed horizontal line in **b** indicates the maximum $B_\perp$ in **c**. We observe oscillatory features that develop at higher $B_\perp$, with their peak and valley positions varying as a function of $B_\perp$, in addition to the field-angle-independent oscillatory features arising from the bulk QWSs. We are however unable to conclusively identify conductance oscillations associated with the LL formation in TSSs, presumably because the conductance is dominated by the bulk-to-bulk tunnelling as both the b- and t-Bi_2Se_3 films are degenerately n-doped. The difference in thickness between the b-Bi_2Se_3 (10 QL) and t-Bi_2Se_3 (20 QL) is responsible for the asymmetry in the periodicity of the QWS-related oscillations at negative and positive biases. All measurements are performed at $T = 0.3$ K.

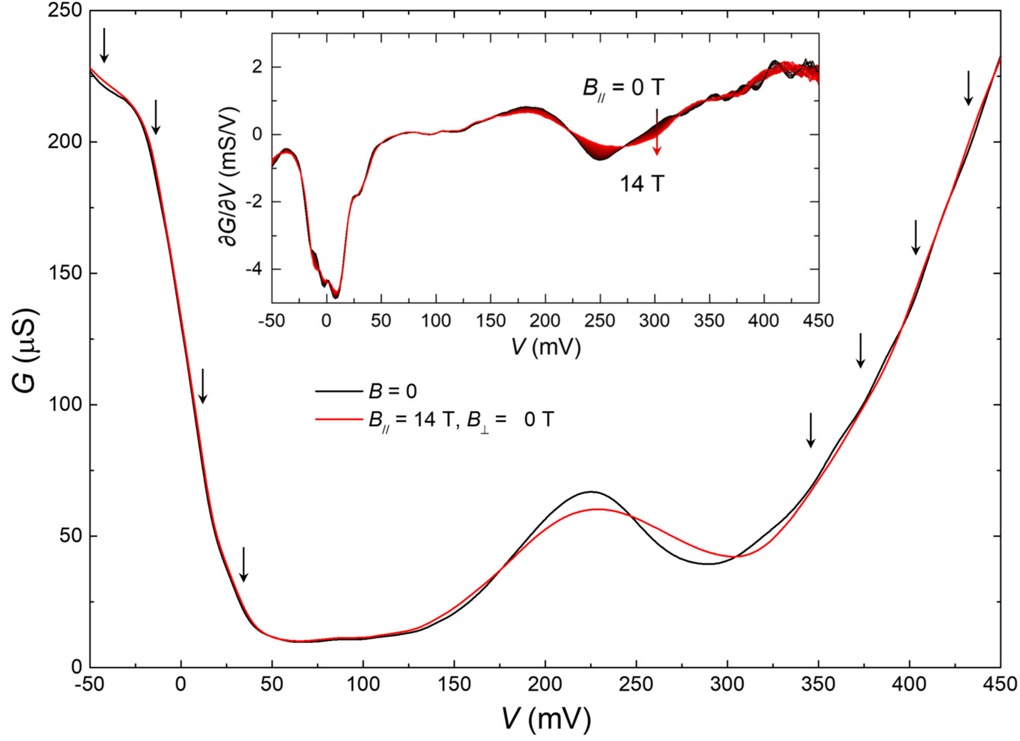

Extended Data Fig. 6. Oscillations in the tunnelling conductance associated with the bulk QWSs. Differential conductance $G(V) = \partial I/\partial V$ of the Bi_2Se_3/2ML hBN/Sb_2Te_3 device at zero magnetic field (black) and $B_{/\!/} = 14$ T (red). The inset shows $\partial G/\partial V = \partial^2 I/\partial V^2$ as a function of V at different $B_{/\!/}$, obtained by taking numerical derivative of $G(V)$. The black arrows indicate the positions of the peaks of the oscillatory feature (I) related to the bulk QWSs, appearing in $\Delta G(V, B)$ (Fig. 4b–e). One can find that they correspond to the valleys of the QWS resonances in $G(V, B = 0)$, which become smoothened out at higher $B_{/\!/}$ as fine structures develop due to the Zeeman effects. We also observe that the $G(V, B = 0)$ peak at $V = 225$ mV, attributed to the alignment of bulk band edges, is suppressed at higher $B_{/\!/}$. All data is measured at $T = 1.8$ K.

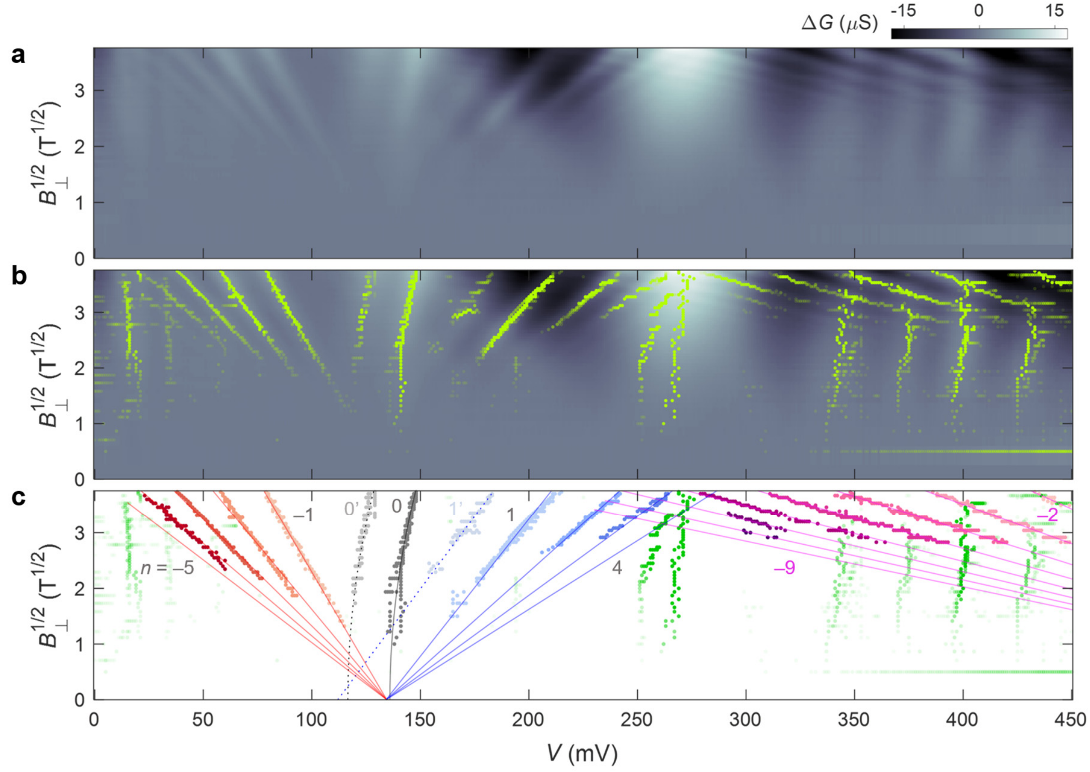

Extended Data Fig. 7. LL peak identifications and LL index assignments. a, Field-modulated component of the tunnelling conductance $\Delta G(V, B)$ at $\theta = 0°$ and $T = 1.8$ K, the same data as Fig. 4b replotted with $B_\perp^{1/2}$ as the vertical axis so that the LLs appear as linear lines. **b**, Peaks identified in **a**. The lime-coloured dots represent the peak positions identified by MATLAB's *findpeaks* function, a tool for locating local maxima, applied along the vertical and horizontal axes, as well as in two diagonal directions. The transparency of the dots corresponds to the prominence of the peaks the function returns. **c**, LL index assignments. The positions of the peaks assigned to each LL index n are indicated by the corresponding colour. The green dots are the positions of the peaks not associated with the LLs. The solid lines tracing the peaks corresponding to $n < 0$ (red) and $n > 0$ (blue) LLs of Sb_2Te_3, and the inter-band inter-LL resonant tunneling between Bi_2Se_3 and Sb_2Te_3 (magenta) are reconstructed from the slopes and intercepts of the linear fits in Fig. 4f. The dark grey curve is a fit to the $n = 0$ LL peaks shifting linearly with respect to $B_\perp$. The dotted curve and line trace the $n = 0$' and 1' LL peaks of unclear origin, respectively.